ARTICLE

Hydrothermal synthesis of hexagonal $YMnO_3$ and $YbMnO_3$ below 250 °C

Received 00th January 20xx,
Accepted 00th January 20xx

DOI: 10.1039/x0xx00000x

Kenneth P. Marshall[a], Sigurd O. Eidem[a], Didrik R. Småbråten[a] *, Sverre M. Selbach[a], Tor Grande[a], Mari-Ann Einarsrud[a]

The hydrothermal synthesis of hexagonal $YMnO_3$ and $YbMnO_3$ are reported using high KOH mineraliser concentrations (>10 M) and low temperatures (< 240 °C). The relation between reaction parameters and resulting phase purity were mapped by *ex situ* and *in situ* X-ray diffraction. Excess Y_2O_3 resulted in two-phase product with hexagonal $YMnO_3$ with different lattice parameters. An unusual microstructure was observed in which particles have a hexagonal shape with a highly crystalline edge and either a hollow or polycrystalline interior. An Oswald ripening mechanism was proposed to explain this phenomenon. Solid-state reactions and density functional theory calculations were performed to determine plausible defect chemistry which can lead to the observed phases with different lattice parameters.

Introduction

Hexagonal manganites are a well-known class of multiferroics, possessing both ferroelectric (Curie temperature > 950 °C) and antiferromagnetic order (Néel temperature ~ 70 K).[1–5] In addition, hexagonal manganites are capable of tolerating oxygen hyper-stoichiometry, giving potential for oxygen storage and oxygen membrane applications.[6–8] As with other piezoelectric materials,[9] hexagonal $YMnO_3$ (h-$YMnO_3$) has been shown to display photocatalytic properties, as Wang *et al.* demonstrated that h-$YMnO_3$ nanoparticles catalysed the degradation of methyl red.[10] In this study, we focus on low temperature synthesis of h-$YMnO_3$ and h-$YbMnO_3$ through hydrothermal synthesis.

h-$YMnO_3$ crystallises in the $P6_3cm$ space group at room temperature and consists of layers of corner sharing MnO_5 triangular-based bipyramids with Y^{3+} in between layers. This is the most thermodynamically stable phase above 789 °C in the Y-Mn-O system.[11] Below this temperature, YMn_2O_5 is the most stable phase. The orthorhombic perovskite phase of $YMnO_3$ (o-$YMnO_3$) becomes more stable than h-$YMnO_3$ at high pressures (~25 GPa), however, the difference in lattice enthalpy between the two phases is small (<1 %) over a wide pressure range (0-35 GPa) according to the model of Jiang *et al.*[12] h-$YMnO_3$ can be converted to o-$YMnO_3$ at high temperature and pressure.[13,14] Oxidising conditions from nitrate precursors during calcination and crystallisation at high temperatures under ambient pressure also favours o-$YMnO_3$.[15,16] At low temperatures o-$YMnO_3$ possesses ferromagnetism (Néel temperature ~ 40 K),[17] and weak ferroelectricity (Curie temperature ~ 30 K).[18]

h-$YbMnO_3$ is isostructural with h-$YMnO_3$, but since Yb has a smaller ionic radius than Y, h-$YbMnO_3$ has smaller lattice parameters than h-$YMnO_3$. The orthorhombic perovskite phase of o-$YbMnO_3$ is less stable (the smaller A-site lowers tolerance factor/geometric stability).

Hydrothermal synthesis, which uses water as a solvent, reaction temperatures above 100 °C and pressures above 1 bar, represents a low temperature route to crystalline materials. A mineraliser is often used to assist in the dissolution and transport of reactants. Dissolved material is able to crystallise when it is supersaturated and the degree of supersaturation has an important effect on the resulting morphology of product particles.[19–21] The degree of supersaturation is defined by the ratio of the product of activities of reactants at a given time to that at the equilibrium condition.[22] h-$YMnO_3$ has been synthesised hydrothermally at < 250 °C from salt precursors, producing nanorod structures,[23] plate-like structures[24] and nanoparticles[25]. Harunsani *et al.*[24] used very high concentration of KOH (9.4 g in 7 mL solution) for the reaction. Using a low concentration[23] or no hydroxide mineraliser[25] have also been reported for the synthesis of h-$YMnO_3$. Stampler *et al.*[26] reported on the synthesis of hexagonal manganites in 3 M KOH from oxide precursors, at temperatures depending on the ionic radius of the rare-earth element, synthesising h-$YMnO_3$ at 350 °C. The hydrothermal synthesis of h-$YbMnO_3$ is simpler due to the lower temperatures required for the reaction as $Yb(OH)_3$ is less stable than $Y(OH)_3$ because the smaller Yb^{3+} cation cannot easily accommodate 9-coordination.[27,28] Our own *in situ* X-ray diffraction (XRD) study on the synthesis of h-$YMnO_3$ at 300 – 350 °C and 1 – 10 M KOH showed that, as well as temperature, the mineraliser concentration plays a

[a] *Department of Materials Science, Norwegian University of Science and Technology, Trondheim, Norway.*

† Footnotes relating to the title and/or authors should appear here.
Electronic Supplementary Information (ESI) available: [details of any supplementary information available should be included here]. See DOI: 10.1039/x0xx00000x

Please do not adjust margins

significant role in the decomposition of $Y(OH)_3$ to the more reactive YO(OH) as an intermediate compound.[29]

Here we report on the hydrothermal synthesis of h-$YMnO_3$ and h-$YbMnO_3$ from oxide precursors (Ln_2O_3 (Ln = Y or Yb) and Mn_2O_3) and h-$YMnO_3$ from salt precursors ($Y(NO_3)_3$, $MnCl_2$, $KMnO_4$). Specifically, we have investigated the low temperature synthesis (≤ 240 °C) with ≥ 10 M KOH mineraliser. From a technical point of view, the low temperature greatly simplifies the synthesis as it allows the use of Teflon® liners for autoclaves, which are highly resistant to corrosion, both under acidic and basic conditions. We have determined the lower KOH concentration ([KOH]) and temperature limits at which h-$YMnO_3$ can form. We then studied the effect of excess Y_2O_3 in the synthesis, which resulted, peculiarly, in two distinct phases of h-$YMnO_3$ with different lattice parameters. The differences in terms of morphology between the two synthesis routes (from oxide and salt precursors), as well as between the higher temperature/lower mineraliser concentration route were also examined. The simple Y_2O_3-H_2O-KOH system was investigated to determine the resulting phases at different [KOH] and temperatures. We have also compared the h-$YbMnO_3$ system to that of h-$YMnO_3$. We have found that single phase h-$YbMnO_3$ was formed below 180 °C, while we do observe two-phase material of h-$YMnO_3$ in the X-ray diffraction patterns at 240 °C, when using both excess Yb_2O_3 and stoichiometric precursors. *In situ* XRD was used to monitor reactions between Y_2O_3 or Yb_2O_3 and Mn_2O_3 at different temperatures to measure the differences between Y and Yb in terms of rate and reaction progression, and to study the impact of addition of $MnCl_2$. Finally, solid-state reactions and density functional theory calculations were performed to further elucidate the effect of non-stoichiometry on the lattice parameters. The results presented cover a wide parameter space and display the substantial differences that temperature, and mineraliser choice and concentration have on outcome of the hydrothermal synthesis of hexagonal manganites in terms of phase purity and morphology.

Results

Effect of reaction parameters

The reaction between Y_2O_3 and Mn_2O_3 during hydrothermal conditions has been studied using stoichiometric precursor mixtures, and with excess Y_2O_3. The reaction with stoichiometric Y_2O_3 and Mn_2O_3 resulted in ~97 wt% h-$YMnO_3$ with YMn_2O_5 as a minor secondary phase (Figure 1 (a), Table s1 reaction Y1). h-$YMnO_3$ synthesised from $Y(NO_3)_3$, $MnCl_2$ and $KMnO_4$ had ~89 wt% phase purity with YMn_2O_5 also as the most prominent secondary phase (Figure 1 (b), Table s1 reaction Y2). h-$YMnO_3$ synthesised from the oxide precursors resulted in a product with lattice parameters close to literature values,[5] while the h-$YMnO_3$ synthesised from salt precursors had significantly larger *a* and smaller *c* parameters (Table 1).

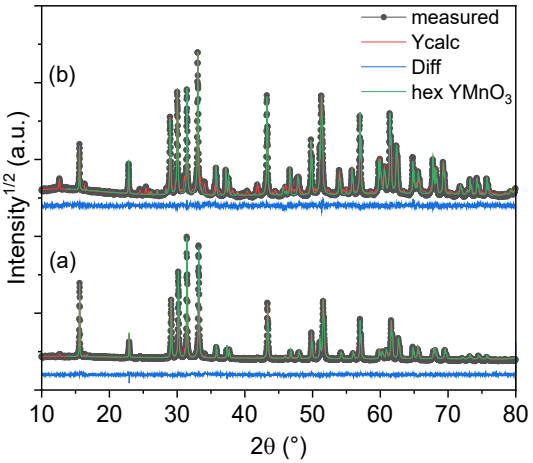

Figure 1: XRD patterns and Rietveld refinement (space group $P6_3cm$) of h-$YMnO_3$ synthesised from (a) stoichiometric Y_2O_3 and Mn_2O_3 in 12.5 M KOH at 240 °C (reaction Y1 in Table s1) and (b) stoichiometric $Y(NO_3)_3$, $MnCl_2$ and $KMnO_4$ solutions in 12.5 M KOH at 240 °C (reactions Y2 in Table s1). Numbers in brackets are errors on the last digit.

To elaborate which synthesis parameters give a phase-pure material, the temperature/[KOH] parameter space was studied to find the effect on the synthesisability of h-$YMnO_3$. The h-$YMnO_3$ phase purity resulting from reactions between Y_2O_3 and Mn_2O_3 with stoichiometric ratios, from 160 to 240 °C for 20 h and 5 to 12.5 M KOH are shown in Figure 2 (a). Generally, higher phase purities were obtained using higher temperatures and [KOH].

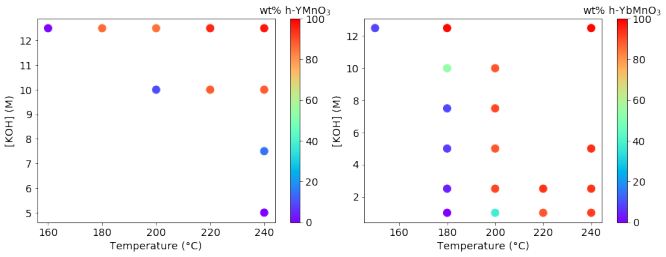

Figure 2: Scatter plot of temperature/[KOH] parameter space for reactions between **(a)** Y_2O_3 and Mn_2O_3 and **(b)** Yb_2O_3 an Mn_2O_3, (1:1 precursors, ~20 h reactions), with the resulting wt% of h-$YMnO_3$ or h-$YbMnO_3$ formed on the colour axis.

When performing the synthesis using 12.5 M NaOH instead of KOH at 240 °C, no h-$YMnO_3$ was formed (Figure S1); only $Y(OH)_3$ and $NaMn_2O_{6-x}$ were observed.

This journal is © The Royal Society of Chemistry 20xx

Please do not adjust margins

Table 1: Lattice parameters of different h-$YMnO_3$ and h-$YbMnO_3$ materials. 12.5 M KOH was used in all cases. Errors on last digit given in brackets.

Material	Time (h)	Reaction number	*a* 1 (Å)	*c* 1 (Å)	*a* 2 (Å)	*c* 2 (Å)
h-$YMnO_3$ literature values[5]			6.14151	11.4013		
Y stoichiometric, 240 °C	20	Y1	6.14038(4)	11.39508(8)		
From $Y(NO_3)_3$, $MnCl_2$ and $KMnO_4$	20	Y2	6.16427(8)	11.37732(8)		
Excess Y, 240 °C	20	Y3	6.1472(1)	11.3879(2)	6.1944(1)	11.3594(3)
Excess Y – 240 °C	63	Y4	6.1527(3)	11.3780(3)	6.1895(2)	11.3572(4)
Y4 heat-treated 1150 °C		Y4b	6.14422(8)	11.4006(2)	6.1637(2)	11.3583(7)
Excess Y, $MnCl_2$ substitution	20	Y16	6.14491(6)	11.3937(1)		
h-$YbMnO_3$ literature values[30]			6.0584	11.3561		
Excess Yb 150 °C	64	Yb3	6.10739(9)	11.3575(3)		
Excess Yb, 180 °C	20	Yb4	6.1011(2)	11.3474(5)		
Yb stoichiometric, 240 °C,	20	Yb6	6.062(2)	11.353(2)	6.0897(3)	11.3600(8)
Excess Yb, 240 °C	20	Yb5	6.0767(9)	11.347(1)	6.0971(2)	11.3571(5)

Effect of excess Y

The use of 15 mol% excess Y in the precursor mixture was studied because of the propensity for the formation of the Y-deficient phase, YMn_2O_5. The use of excess Y resulted in two distinct phases of h-$YMnO_3$ with different lattice parameters; a low-*a*, high-*c* lattice parameter phase and a high-*a* and low-*c* parameter phase, which is manifested by the appearance of peak splitting in the XRD patterns. Figure 3 compares the XRD patterns of h-$YMnO_3$ formed using excess Y for 20 and 63 h compared to a product formed under stoichiometric conditions (reactions Y3, Y4 and Y1 in Table s1, respectively). Secondary phases of YMn_2O_5, $Y(OH)_3$ and KMn_2O_{6-x} were also present after 20 h, however, no YMn_2O_5 was observed after 63 h. Lattice parameters for the h-$YMnO_3$ products are included in Table 1. The single h-$YMnO_3$ phase, resulting from the stoichiometric precursors, has a smaller *a* lattice parameter and larger *c* lattice parameter, closer to literature values,[5] than both phases observed in the product of the excess Y reaction.

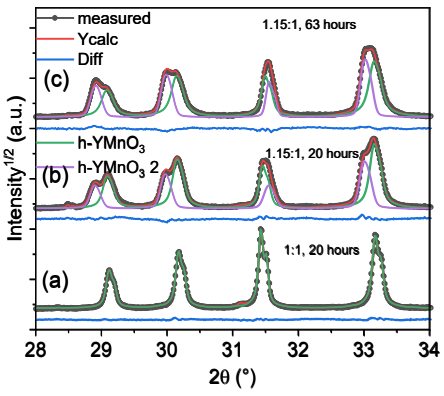

Figure 3: XRD patterns and Rietveld refinements (space group $P6_3cm$) of h-$YMnO_3$ synthesised hydrothermally at 240 °C in ~12.5 M KOH with **(a)** stoichiometric precursors (20 h), **(b)** 15 mol% excess Y (20 h), and **(c)** 15 mol% excess Y (63 h). Reactions Y1, Y3 and Y4 in Table s1. Components shown: two calculated h-$YbMnO_3$ phases (green and purple), total fit (red), measured pattern (black circles), and difference between the measured pattern and fit (blue).

Our preliminary hypothesis was that the two h-$YMnO_3$ phases had different oxygen stoichiometries, as tolerance for excess oxygen in hexagonal manganites and the effect this has on the lattice parameters is well documented (increase in *a*, reduction in *c*), due to the ability for Mn(III) to oxidise to Mn(IV).[6,8] However, after conducting *in situ* heating experiments on the powder, it was found that the peak splitting resulting from different *a* parameters did not disappear on heating to 600 °C, although the *c* parameters appeared to have converged on cooling (Figures S2 (a) and (b)). *Ex situ* XRD showed that peak splitting had not completely disappeared after heating to 1150 °C. The *a* parameters were reduced in both phases, while the *c* parameter was significantly increased in one of the phases. Significant amounts of Y_2O_3 also appears in this powder (Table 1 reaction Y4b, Figure S2 (c)). The two distinct h-$YMnO_3$ phases likely have different Y:Mn ratios, though it is unclear why they form. On heating to 1150 °C, there is diffusion of Y out of non-stoichiometric $YMnO_3$, forming Y_2O_3, leading to the observed lattice parameter changes. Fedorova *et al.* reported that the h-$YMnO_3$ system is capable with tolerating excess Y, at least above 900 °C .[31] However, it is not stated if the samples retained the non-stoichiometry on cooling to room temperature. Under reducing conditions in which 5 mol% $MnCl_2$ is substituted for Mn_2O_3 (by mole of Mn) (reaction Y16), only a single phase of h-$YMnO_3$ is observed with lattice parameters close to the literature values[5] (compared with values in the high *a*, low *c* phases in other samples) (Table 1).

Particle morphology

h-$YMnO_3$ formed from Y_2O_3 and Mn_2O_3 at 240 °C and > 10 M KOH have a hexagonal prism shape (Figure 4 (a) and (b)), often with hollow or rough interior compared to those made at high temperature (≥ 300 °C) and moderate mineraliser concentration (≤ 5 M), as shown in our previous work where hexagonal plate like morphologies were formed.[29] The crystals prepared at 240 °C and > 10 M KOH from the salt precursors have a polygonal plate-like

morphology, often with a hollow or partially hollow centre (Figure 4 (c)).

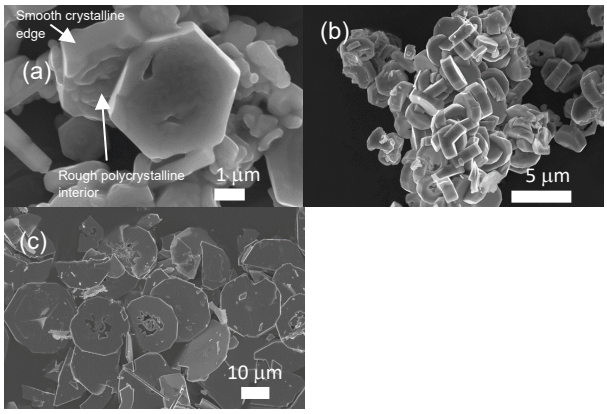

Figure 4: SEM images of h-$YMnO_3$ synthesised from Y_2O_3 and Mn_2O_3 at 240 °C in ~12.5 M KOH with **(a)** stoichiometric precursors (~ 20 h) (reaction Y1), **(b)** 15 mol% excess Y_2O_3 (~ 20 h) (reaction Y3) and **(c)** h-$YMnO_3$ synthesised from $Y(NO_3)_3$, $MnCl_2$ and $KMnO_4$ (~ 20 h), (reaction Y2).

To investigate the mechanism for the particle hole formation, the reaction between $Y(NO_3)_3$, $MnCl_2$ and $KMnO_4$ was performed at 240 °C for 6 to 72 h, and the particle and hole sizes were measured from each sample using SEM. There was no correlation between reaction time and particle size. There appears to be a larger proportion of particles with holes as the reaction time increases, however, there is no obvious correlation between the sizes of holes and reaction time from 24 h onwards (Figures S3 and S4).

h-$YbMnO_3$

The synthesis of h-$YbMnO_3$ from Yb_2O_3 and Mn_2O_3 was studied in the temperature range 120 – 240 °C using 1 to 12.5 M KOH. h-$YbMnO_3$ can be formed under milder conditions than h-$YMnO_3$ as the data in Figure 2 show; > 80 wt% h-$YbMnO_3$ was synthesised at 1 M KOH and 240 °C, whereas no h-$YMnO_3$ formed at 5 M KOH and 240 °C. The reactions at 180 °C and 240 °C in 12.5 M KOH with 15 mol% excess Yb_2O_3 yielded phase purities of ~ 99 wt% after 20 h. The same reaction at 150 °C resulted in h-$YbMnO_3$ with a phase purity of ~9 wt%, with secondary phases of YbO(OH) and Mn_2O_3 after 20 h. At ~64 h this reaction gave 88 wt% h-$YbMnO_3$, and the reaction at 120 °C for 7 days resulted in ~7 wt% h-$YbMnO_3$ with unreacted YbO(OH) and Mn_2O_3 comprising the rest of the product. At 240 °C, two-phase h-$YbMnO_3$ was obtained as seen from the diffractograms in Figure 5, both when using excess Yb and stoichiometric precursors. Unlike in the case of h-$YMnO_3$, the two phases were observed when using stoichiometric precursors, as well as when using excess Yb. Lattice parameters of the h-$YbMnO_3$ phases included in Table 1 show that when excess Yb is used, the *a* lattice parameters are consistently larger than the values reported by van Aken *et al.*[30] (*a* = 6.0584 Å, *c* = 11.3561 Å), however, when stoichiometric Yb:Mn precursors are used, one phase has an *a* lattice parameter closer to the reported value, although there is also a second h-$YbMnO_3$ phase present with larger lattice parameters. This may be an indication of excess Yb in the structure analogue to what was observed for h-$YMnO_3$, Fedorova *et al.* showed that h-$YbMnO_3$ tolerates excess Yb above 900 °C.[32] All reactions from stoichiometric Yb_2O_3 and Mn_2O_3 using ≤ 10 M KOH resulted in no peak splitting in the diffractograms of the resulting h-$YbMnO_3$.

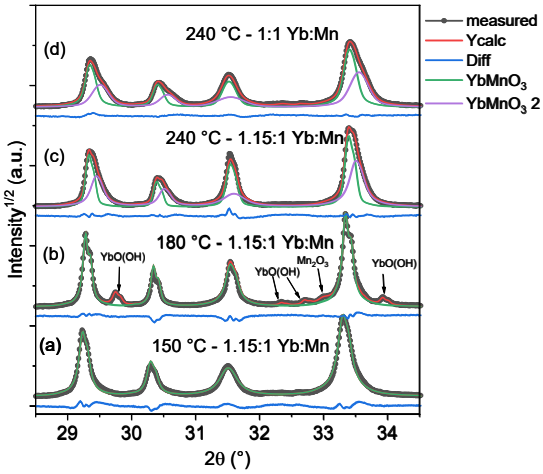

Figure 5: XRD patterns and Rietveld refinements (space group *P*6$_3$*cm*) of h-$YbMnO_3$ synthesised from Yb_2O_3 and Mn_2O_3 using 15 mol% excess Yb in 12.5 M KOH at **(a)** 150 °C for 64 h (reaction Yb3) and **(b)** 180 °C for 20 h. h-$YbMnO_3$ synthesised at 240 °C for 20 h in 12.5 M KOH (reaction Yb4) with **(c)** 15 mol% excess Yb_2O_3 (reaction Yb5), and **(d)** stoichiometric precursors (reaction Yb6). Components shown: two calculated h-$YbMnO_3$ phases (green and purple), total fit (red), measured pattern (black circles), and difference between the measured pattern and fit (blue).

Y_2O_3 in KOH

We now turn to the impact that mineraliser (KOH) concentration has on the Y_2O_3-$Y(OH)_3$-YO(OH) system, finding that higher temperatures and [KOH] generally leads to greater fractions of YO(OH) and smaller fractions of Y_2O_3. However, when no KOH was present, more YO(OH) was observed than at low or moderate [KOH]. Weight fractions of Y_2O_3, $Y(OH)_3$, and YO(OH) under different conditions are shown in Figure 6. This is in line with our previous *in situ* study on the synthesis of h-$YMnO_3$.[29]

This journal is © The Royal Society of Chemistry 20xx

Please do not adjust margins

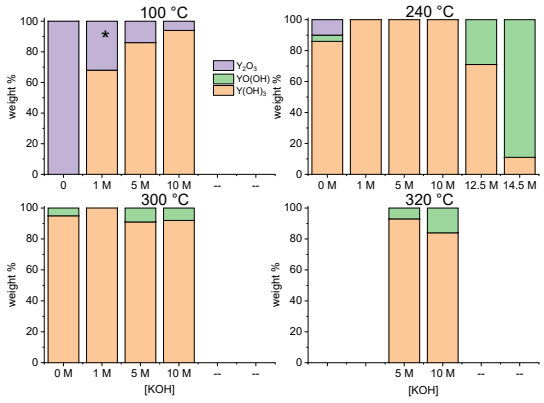

Figure 6: Bar graphs of weight fractions of phases from the reaction of Y_2O_3 in KOH solutions of different concentrations for 5 h; 0, 1, 5, 10, 12.5, and 14.5 M, and at different temperatures; **(a)** 100, **(b)** 240, **(c)** 300 and **(d)** 320 °C. *At 1 M KOH and 100 °C an unknown phase appeared.

Kinetics

In situ measurements of hydrothermal reactions between Y_2O_3 or Yb_2O_3 and Mn_2O_3 were made using synchrotron XRD. Kinetic data from these studies are shown in figures 7 and 8, with phase evolution data shown in Figure S8. Figure 7 shows the evolution of h-$LnMnO_3$ over reaction time (circles and lines) along with the corresponding fits modelled using the Avrami model,[33,34] which has some history in the interpretation of hydrothermal kinetic data,[35] (solid lines); $Y = 1 - e^{-Kt^n}$, where Y is the extent of reaction, K is the rate constant, and n is an exponent related to the reaction mechanism and crystal growth dimensionality.[33,35] The extent of reaction was determined from the Rietveld refined scale factor of h-$YMnO_3$ which was normalised to the scale factor at the end of the reaction. The sudden change in rates for Yi1 (240 °C) and Yi4 (300 °C) visible in Figures 7 (a) and (c) coincide with the exhaustion of Mn_2O_3 and a change of reaction mechanism from which $Y(OH)_3$ or YO(OH) and Mn_2O_3 directly to one where the Y compounds react with YMn_2O_5 which is much slower due to the higher thermodynamic stability and lower solubility product of the YMn_2O_5 compared with Mn_2O_3. The ln(K) values extracted from the fits are plotted against 1/T in Figure 8 for different reactions. The time = 0 point was chosen for each reaction such that n = 2.5 for every reaction so that the K values were comparable. These data show that the reaction rates at 270 and 300 °C are independent of whether Y or Yb are used in the reaction. Additionally, when Y_2O_3 is used, the addition of $MnCl_2$ has no impact on the reaction rate, although it does substantially impact the resulting phase purity (Figures S8 (a) and (b), Table s1 reactions Yi1 and Yi2). However, the rate of reaction between Yb_2O_3 and Mn_2O_3 at 240 °C is substantially impacted by $MnCl_2$, with the reaction occurring much faster; the reaction rate is similar to the reaction without $MnCl_2$ at 270 °C.

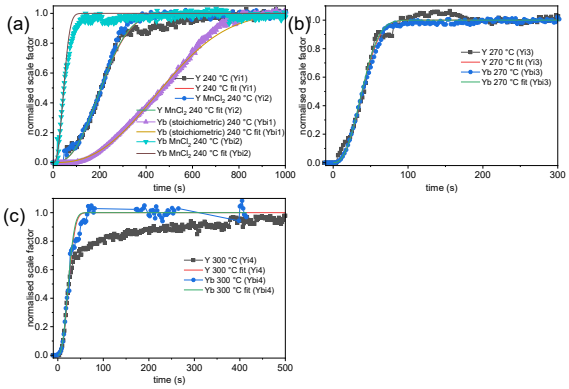

Figure 7: Evolution of the scale factor of h-$YMnO_3$ over time for the reaction between Y_2O_3 or Yb_2O_3 and Mn_2O_3 with 15 mol% excess Y or Yb **(a)** with and without $MnCl_2$ added to the reaction at 240 °C (Table s1: Yi1, Yi2, Ybi1, Ybi2), **(b)** at 270 °C (Yi3, Ybi3), **(c)** at 300 °C (Yi4, Ybi4). All reactions were done in 10 M KOH. Measured data shown by line and symbol, fits shown by solid lines.

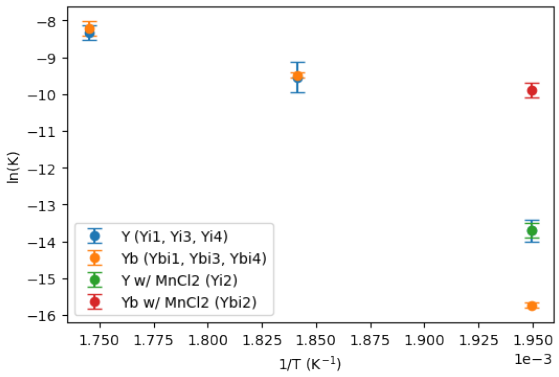

Figure 8: ln(K) plotted against 1/T, where K is the rate constant and T is temperature for the reaction between Y_2O_3 or Yb_2O_3 and Mn_2O_3 in 10 M KOH with 15 mol% excess Y or Yb unless otherwise stated. Data taken using fitting parameters from Figure 7 (reactions Yi1 – Yi4 and Ybi1 – Ybi4 in Table s1).

Discussion

Parameter space for $YMnO_3$ synthesis

Generally, high phase purity h-$YMnO_3$ can be achieved using high temperatures and high [KOH]. From the parameter space studies between 160 and 240 °C and 2.5 and 12.5 M KOH, at least 10 M KOH and 220 °C are required to achieve > 90 wt% phase purity. It is worth noting that there have been reports of low mineraliser concentration reactions at 240 °C,[23,25] however, we have not been able to reproduce these results. Additionally, the mineraliser type is important; we see h-$YMnO_3$ forms when using KOH, but not using NaOH at the same concentrations. The formability is related to the stability of the $Y(OH)_3$ transient phase, which itself is dependent on

Please do not adjust margins

these factors; higher temperatures and [KOH] leads to more dehydration of $Y(OH)_3$ to YO(OH), and more hydration of Y_2O_3 to $Y(OH)_3$ (Figure 6). It is also evident that at 240 and 300 °C, in the absence of KOH, more YO(OH) forms than with low or moderate [KOH]. We also observed a similar effect in our previous *in situ* study, in which 1 M KOH at 320 °C caused the concurrent formation of YO(OH) and $Y(OH)_3$ during the reaction between Y_2O_3 and Mn_2O_3, whereas with 5 M KOH, much less YO(OH) was formed, and it only appeared after the appearance of $Y(OH)_3$. This suggests that in the absence or in low concentrations of KOH mineraliser, there can be a 1-step formation of YO(OH) from Y_2O_3, whereas at higher KOH concentrations, a 2-step formation of YO(OH) (via $Y(OH)_3$) occurs. Figure 2 then shows how this translates into h-$YMnO_3$ formation; there is a clear trend that high temperature and [KOH] lead to higher h-$YMnO_3$ phase purities. However, h-$YMnO_3$ was formed under conditions that were too mild to form YO(OH) from Y_2O_3 in KOH solution. Our *in situ* study did show that YO(OH) was present under milder conditions in the reaction between Y_2O_3 and Mn_2O_3 in KOH solution, compared with only Y_2O_3 in KOH solution.[29]

Microstructure

The microstructure of h-$YMnO_3$ is different in the low temperature (≤ 240 °C), high [KOH] (≥ 10 M) region of parameter space (Figure 4) from the high temperature (≥ 300 °C) moderate [KOH] (≤ 10 M) as we have seen in our prior work, in which we observed thin hexagonal crystals ~ 10 □m across.[29] In the case of using the oxide precursors, thick plate-like structures, often with rough or porous interiors are formed, and in the case of using salt precursors, thin plate-like structures often with holes in the centre are formed.

Both may have similar origins, with the different shapes originating from different precursor particle sizes. One possible explanation is an Ostwald ripening mechanism in which a polycrystalline core dissolves while the more crystalline particle edge grows. Support for this mechanism for the material synthesised by the oxide route can be seen in the SEM image in Figure 4 (a), in which thick plate-like particles can be seen with rough, polycrystalline cores and smoother, more crystalline edges (annotations in figure). This type of mechanism has been widely reported for hollow circular and spherical polycrystalline particles.[36–38] A schematic of the Oswald ripening mechanism is shown in Figure 9.

An alternative mechanism for the hole formation was described by Budhysutanto *et al.* for the preparation of Mg-Al double hydroxide.[39] In their work, they suggested that hollow plate-like crystals formed by a large difference in solubility of two precursors, with the more soluble precursor depositing around the less soluble one, causing the reaction, and the less soluble precursor gradually eroded. This mechanism is an attractive possibility considering the resemblance between their Mg-Al hydroxide particles with the h-$YMnO_3$ synthesised by the salt route (Figure 4 (c)). Y:Mn ratios measured by energy dispersive X-ray spectroscopy (EDX) did not show any obvious gradients, either within a sample, or between different samples (Figures S5 and S6), showing that this mechanism is less likely to occur. A time-dependent study on the h-$YMnO_3$ synthesis using salt precursor, showed that after 6 h, the reaction was mostly complete, while all the thin plate-like particles were found to be dense. It was only samples that had been reacted for longer time that holes appeared (holes observed at 24 h), suggesting that the hole forms after the initial reaction (Figures S3 and S4).

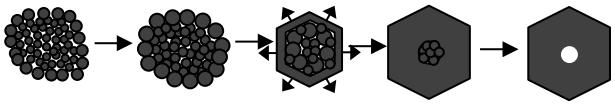

Figure 9: Suggested mechanism for the formation of hollow plate-like particles (such as in Figure 4(c)) by Ostwald ripening followed by crystal growth.

Two-phase materials

The formation of two h-$YMnO_3$ phases in the reaction between excess Y_2O_3 and Mn_2O_3 is likely the result of different particles with different Y:Mn ratios in the final structures, whether manifested by manganese vacancies or yttrium antisites. Based on the lattice parameters, it appears that both phases of h-$YMnO_3$ have an excess of Y, but to different extents. It is also uncertain if the Y:Mn non-stoichiometry exists throughout the reaction, or if the excess Y is incorporated into the structure later. Interestingly, under reducing conditions, but with excess Y (reaction Y16), we do not observe two phases of h-$YMnO_3$, which implies that oxidation of Mn is also an important factor. The *ex situ* powder diffraction pattern of a two-phase h-$YMnO_3$ sample synthesised from Y_2O_3 and Mn_2O_3 (1.15:1) in 12.5 M KOH (repeat of Y3) was measured using synchrotron radiation to get better resolution and signal to noise than is possible from a lab diffractometer (zoom of the refined pattern shown in Figure S9). The refined Mn occupancies and lattice parameters are reported in Table 2. These data show that the difference in lattice parameters from those of the stoichiometric phase[5] correlates with a reduction in the relative amount of Mn in the structure.

Table 2: Refined lattice parameters and Mn occupancy of two h-$YMnO_3$ phases from a hydrothermally synthesised sample from synchrotron XRD data. Error on last digit in brackets.

Phase	a (Å)	c (Å)	Mn occupancy
h-$YMnO_3$ 1	6.1501(2)	11.3782(4)	0.886(7)
h-$YMnO_3$ 2	6.1917(2)	11.3524(4)	0.728(6)

To clarify the effect of excess Y on bulk h-$YMnO_3$ for comparison with the samples in Table 1, a series of $Y_{1+x}MnO_3$ materials with x = 0, 0.014, 0.042 and 0.083 was prepared by solid-state reaction and investigated by laboratory XRD and Rietveld refinement with results presented in Table 2. Compositions were chosen to match the supercell stoichiometries for the DFT calculations presented below. Full series of XRD patterns are presented in the Supplementary Information (Fig. S7). Compared to hydrothermal synthesis, the solid-state reaction method offers excellent control of nominal cation stoichiometry and the clear trend is that excess Y expands both lattice parameters *a* and *c*. This supports the hypothesis that the two

 This journal is © The Royal Society of Chemistry 20xx

Please do not adjust margins

Table 3: Refined lattice parameters of solid-state prepared h-$Y_{1+x}MnO_3$ materials with different cation stoichiometries. Errors on last digits given in brackets

x in h-$Y_{1+x}MnO_3$	*a* (N_2) (Å)	*c* (N_2) (Å)	*a* 1 (O_2) (Å)	*c* 1 (O_2) (Å)	*a* 2 (O_2) (Å)	*c* 2 (O_2) (Å)
0.000	6.13833(5)	11.3961(1)	6.13880(5)	11.3934(1)	6.2042(6)	11.085(1)
0.042	6.14319(7)	11.4168(1)	6.15339(9)	11.3863(2)	6.1867(2)	11.2432(7)
0.167	6.14414(6)	11.4228(1)	6.1609(2)	11.3701(4)	6.1885(2)	11.2405(5)

phases observed have different lattice parameters as a consequence of different cation stoichiometries. To assess the effect of oxygen stoichiometry, XRD was performed after heat-treating the solid-state samples in flowing N_2 at 1000 °C and O_2 at 300 °C, respectively. The refined lattice parameters are presented in Table 3 and show that regardless of the atmosphere, Y excess induces expansion of the *a* lattice parameter. Interestingly, an expansion of the *c* lattice parameter with Y excess in N_2 is observed, while a contraction is observed in O_2. After the oxidation under O_2 flow at 300 °C, two h-$YMnO_3$ phases, with large differences in lattice parameters, especially *c*, are observed in the samples due to differing degrees of oxidation in different particles within the samples. The sample synthesised with 16.7 % excess Y also contained significant Y_2O_3 after heat treatments: 6 wt% after N_2 annealing, and 8 wt% after oxidising in O_2 as determined by Rietveld refinement.

As the point defects resulting from Y excess are not known, DFT calculations were performed where the geometries were optimised for $Y_{1+x}MnO_3$ supercells with the same x values as the solid-state samples. Two different scenarios were investigated as described in Kröger-Vink notation;

1. Y excess caused by Mn vacancies:

$$\frac{1}{2}Y_2O_3 + 3Mn_{Mn}^{\times} \xrightarrow{YMn_{1-x}O_3} Y_Y^{\times} + V_{Mn}^{'''} + 3Mn_{Mn}^{\bullet} + 3O_O^{\times}$$

2. Y excess caused by Mn on Y sites:

$$\frac{1}{2}Y_2O_3 \xrightarrow{Y_{1+x}Mn_{1-x}O_3} Y_{Mn}^{\times} + \frac{3}{2}O_O^{\times}$$

The relaxed lattice parameters presented in Table 4 show that both scenarios are predicted to expand the lattice parameters of h-$YMnO_3$. Comparison with the experimental data in Table 2 is non-trivial as it is not known from experiment what the different stoichiometries of the two phases are. It can thus not be ruled out that both Mn vacancies and Y antisites are present, but in different concentrations as DFT predicts Y antisites to give a much stronger expansion than Mn vacancies. The reason for this difference is that Y^{3+} is larger than Mn^{3+}, causing a strong expansion of the lattice. Here, Mn vacancies are charge compensated by oxidising three adjacent Mn^{3+} (0.58 Å, C.N. = 5) to Mn^{4+} (0.46 Å, C.N. = 5, interpolated)[40] rather than with oxygen vacancies, which would also contribute to lattice expansion.[41] Oxygen-rich conditions where a fraction of Mn^{3+} is oxidised to Mn^{4+} was deemed more relevant to hydrothermal conditions than compensating Mn vacancies by oxygen vacancies.

Table 4: DFT calculated lattice parameters for different concentrations (x) and mechanisms of Y excess.

x in h-$Y_{1+x}MnO_3$	*a* (V_{Mn}) (Å)	*c* (V_{Mn}) (Å)	*a* (Y_{Mn}) (Å)	*c* (Y_{Mn}) (Å)
0.000	6.0996	11.4216	6.0996	11.4216
0.042	6.1016	11.4203	6.1087	11.4702
0.167	6.1136	11.4281	6.1346	11.6316

The appearance of two phases was observed also when h-$YbMnO_3$ was synthesised at 240 °C, both when prepared using excess Yb_2O_3 and for stoichiometric precursors, however the two phases were not observed at lower temperatures (≤ 220 °C). The *a* lattice parameters, however, were consistently higher compared with reported values when using excess Yb_2O_3. Just as with the h-$YMnO_3$, we propose that this is the result of non-stoichiometry between Yb and Mn in the structure, although it is unclear how the two-phase system forms. Jeuvery *et al.*[40] synthesised h-$YMnO_3$ with up to 10 mol% excess yttrium and found that both lattice parameters increased up to an excess of approximately 5 mol% yttrium in the precursor. The *a* parameter was found to increase from 6.135 Å to 6.141 Å, and the *c* parameter from 11.387 Å to 11.396 Å. Here, we have observed much larger differences in lattice parameters, with *a* parameters ranging from 6.140 Å to 6.189 Å across all samples, and from 6.145 Å to 6.186 Å within a single sample (Table 1).

Comparison of yttrium and ytterbium systems

The synthesis of h-$YbMnO_3$ was investigated with [KOH] from 1 to 12.5 M, and temperature from 120 to 240 °C. A lower temperature was used in the reaction because the $Yb(OH)_3$ – YbO(OH) transition temperature is lower compared with that in the Y system. Additionally, the $YbMn_2O_5$ secondary phase does not form as easily as YMn_2O_5, which makes longer reaction times feasible for improving phase purity under mild conditions. However, the kinetics are very

Please do not adjust margins

different as the low temperatures reduce the overall rate of the reaction; we observed that the reaction at 150 °C and 12.5 M KOH still had unreacted precursor after > 60 h reaction, and at 120 °C very little h-$YbMnO_3$ had formed after 7 days, even though the dehydration of $Yb(OH)_3$ to YbO(OH) did occur. The hydroxide to oxyhydroxide transition is therefore not the only factor determining the formability of hexagonal manganites, and precursor solubility and diffusion length are clearly important factors as well.

Kinetics and reaction progression

In situ X-ray diffraction was used to probe reactions between Y_2O_3 or Yb_2O_3 and Mn_2O_3 in 10 M KOH between 240 and 300 °C. From the phase evolution data in Figure S8, all reactions with Yb_2O_3 progressed via YbO(OH) without the appearance of $Yb(OH)_3$, whereas the Y_2O_3 reactions either subsequently progressed from $Y(OH)_3$ to YO(OH) (at 270 and 300 °C, or no YO(OH) was observed and h-$YMnO_3$ appeared directly from $Y(OH)_3$ intermediate. At 270 and 300 °C there is little difference in the rates of reaction between Yb_2O_3 and Y_2O_3, however at 240 °C, larger differences appear. It is difficult to explain why the Yb_2O_3 reactions with and without $MnCl_2$ behave so differently, while the reaction between Y_2O_3 and Mn_2O_3 is affected little in terms of rate on addition of $MnCl_2$.

Two-phase h-$YMnO_3$ was only observed during one *in situ* reaction which was performed at 270 °C (Yi3). The two phases appear to grow concurrently in the early phase of the reaction, but the proportion of the minority h-$YMnO_3$ phase continues increasing at the expense of the majority h-$YMnO_3$ phase after the reactants have been depleted. In this case the minority phase had the smaller *a*-parameter and larger *c*-parameter, i.e. the phase closer to stoichiometric Y:Mn ratio (h-$YMnO_3$ 1 in tables and figures). This indicates that the two phases were not in equilibrium, and that Y may have been leaching out from the large *a* small *c* phase (h-$YMnO_3$ 2 in tables and figures).

Conclusions

We have investigated the hydrothermal synthesis of h-$YMnO_3$ and h-$YbMnO_3$ below 250 °C with 12.5 M KOH. Considerable differences were observed between the reaction products when using stoichiometric precursors and excess Y; with excess Y two distinct phases of h-$YMnO_3$ with different lattice parameters form. This likely results from different Y:Mn stoichiometries in the two h-$YMnO_3$ phases. This explanation is supported both by complimentary DFT calculations, refinements of *in situ* and *ex situ* synchrotron powder XRD data, and studies on Y rich bulk samples prepared by solid-state reaction. Additionally, the morphologies are considerably different from h-$YMnO_3$ synthesised at > 300 °C and in 5 M KOH, which has a hexagonal plate morphology, and from that synthesised at 240 °C in 12.5 M KOH from salt precursors, which has a plate structure, often with a hollow centre. There is a definite link between $YMnO_3$ formability and temperature and mineraliser concentration, which is in turn related to the stability of $Y(OH)_3$ and its transition to YO(OH). The two-phase system is observed generally both for h-$YMnO_3$ and h-$YbMnO_3$ when using high temperatures and KOH concentrations.

Experimental

Hydrothermal synthesis:

Mn_2O_3 (99 %, Sigma Aldrich) heat-treated at 600 °C to reduce MnO_2 secondary phase visible from XRD, Y_2O_3 (99.9 %, Alpha Aesar), Yb_2O_3 (99.9 %, Sigma Aldrich), $Y(NO_3)_3.6H_2O$ (99.8 %, Sigma Aldrich), $MnCl_2.4H_2O$ (99 %, Sigma Aldrich), $KMnO_4$ (99.0 % Sigma Aldrich), and KOH (Sigma Aldrich, 90 wt%) were used in this study.

Synthesis from oxide precursors was performed by mixing Y_2O_3 (0.371 or 0.426 g) or Yb_2O_3 (0.647 or 0.744 g) (1:1 or 1.15:1 molar ratio with Mn_2O_3, respectively) and Mn_2O_3 (0.259 g), with a pestle and mortar until the mixture formed a uniform grey colour. These were then added to a 23 mL Teflon lined steel autoclave. To this, water (7 or 9 mL) was added (for 14.5 M and 12.5 M solutions respectively), followed by addition of KOH flakes (10 g) over the course of 30 min (KOH had not fully dissolved at this point). The autoclave was then sealed and transferred to a preheated oven and heated for the given reaction time and removed while hot. Powders were collected by filtration, washed with deionised water, and dried for ~5 h at 110 °C, then ground using a pestle and mortar. A summary of different reactions is shown in Table s1. Reaction Y16, in which Y_2O_3, Mn_2O_3 and $MnCl_2$ were added in an ionic ratio of 1.15:0.95:0.05, was prepared similarly: Y_2O_3 (0.426 g) and Mn_2O_3 (0.246 g) were ground together with a pestle and mortar, then added to a Teflon® liner. $MnCl_2.4H_2O$ (0.016 g) was then added, followed by deionised water (9 mL) and KOH (10 g). The reaction was performed at 240 °C for 20 h.

The heat-treatment of 2-phase h-$YMnO_3$ was performed at 1150 °C for 5 h using heating and cooling rates of 200 °C/h using a Nabertherm furnace.

For reactions of Y_2O_3 in KOH solutions below 250 °C, stock solutions (10 mL) were used to for reactions involving 1, 5 or 10 M KOH, and higher concentrations were prepared using solid KOH. Above this temperature, a 100 mL Monel (Ni/Cu alloy) autoclave was used with 20 mL of solution. Reactions were run for 5 h.

Synthesis of h-$YMnO_3$ from $Y(NO_3)_3$, $MnCl_2$ and $KMnO_4$ was done using stock solutions of concentrations 0.50, 0.50, and 0.12 M, respectively in a 5:4:1 molar ratio, similar to the method of Harunsani *et al*.[24] $Y(NO_3)_3$ solution (3 mL) and $KMnO_4$ (2.5 mL) were added to a Teflon liner, to this, deionised water (1 mL) was added, and then KOH flakes (10 g) over the course of 30 mins. After this $MnCl_2$ solution (2.4 mL) was added, turning the solution brown in colour. The reactions were performed at 240 °C for ~ 20 h. A summary of this reaction (Y2) is included in Table s1.

In situ X-ray diffraction data were taken at The Swiss-Norwegian beamlines (BM01) at ESRF, Grenoble, France. A 0.73074 Å wavelength beam was used. Reactions were performed in sapphire capillaries with pressure provided using an HPLC pump connected via steel tubing and Swagelok® parts.[29,41] The capillary was held by a

 This journal is © The Royal Society of Chemistry 20xx

Please do not adjust margins

Please do not adjust margins

custom-built cell attached to a goniometer head. Reaction codes in Table s1 containing an 'i' denote *in situ* reactions.

X-ray diffractograms were recorded on a Bruker D-8 Focus with Cu $K\alpha_1$ and $k\alpha_2$ radiation, with a small amount of $K\beta_1$. The emission profile was calibrated with a LaB_6 standard. The detector was a LynxEye SuperSpeed Detector. Rietveld refinements were performed using Topas 5.[42] Scanning electron microscopy was done using a Zeiss Supra 55 VP microscope. Crystallographic information files used for refinements: h-$YMnO_3$ ($P6_3cm$),[5] h-$YbMnO_3$ ($P6_3cm$),[30] $Y(OH)_3$ ($P6_3/m$),[43] YO(OH) ($P12_1/m1$),[44] YMn_2O_5 ($Pbam$),[45] KMn_2O_{6-x} ($P6_3/mmc$),[46] YbO(OH) ($P12_1/m1$).[47]

Solid-state reaction:
$Y_{1+x}MnO_3$ bulk powders were prepared by conventional solid-state reaction. Dried Y_2O_3 (99.99 %, Sigma Aldrich) and Mn_2O_3 (99 %, Sigma Aldrich) were mixed in ethanol in a mortar. Uniaxially pressed (40 MPa) pellets (Ø=15 mm) were fired in air at 1450 °C for 12 h. Next, bulk powders from crushed pellets were annealed at 1000°C in N_2 (g) flow for 1h and quenched to room temperature. Subsequently, the bulk powders were heated in O_2 (g) flow at 300°C for 1 h to oxidise, and subsequently cooled to room temperature at a rate of 4.1°C/h. X-ray diffractograms were recorded after each heat treatment using a Bruker Davinci-1 diffractometer with Cu K_α radiation collecting data for 1h over 10-75° 2θ. Rietveld refinements were performed using Topas 5.[42], with initial crystallographic data from ref. [5].

Computational details:
Density functional theory calculations were carried out using VASP[48–50]. Y (4s, 4p, 5s), Mn (3s, 3p, 3d, 4s) and O (2s, 2p) were treated as valence electrons, with a plane-wave cut-off energy of 550 eV. A combination of PBEsol+U[51,52] with U=5 eV on Mn 3d and a frustrated anti-ferromagnetic ordering on the Mn sublattice was used to reproduce the experimental lattice parameters[4] and the electronic band gap.[53] Brillouin zone integration was performed on a Γ-centered *k*-point grid with a density of 4x4x2 for the 30 atoms unit cells, and 2x2x2 for the 120 atom 2x2x1 supercells. Lattice parameters and atomic positions were relaxed until residual forces on all atoms were below 0.005 eV/Å. One manganese vacancy or Y antisite per supercell were introduced, corresponding to the stoichiometries $YMn_{1-x}O_3$ or $Y_{1+x}Mn_{1-x}O_3$, respectively, with x=1/6 (~0.167) for the unit cell calculations and x=1/24 (~0.042) for the 2x2x1 supercell calculations.

Author Contributions

We strongly encourage authors to include author contributions and recommend using CRediT for standardised contribution descriptions. Please refer to our general author guidelines for more information about authorship.

Conflicts of interest

There are no conflicts to declare.

Acknowledgements

The authors would like to thank the Research Council of Norway (project numbers: 250403, 231430 and 275139) and NTNU for funding. Computational resources for DFT calculations were provided by Uninett Sigma2 through the project NN9264K. We would also like to thank the Swiss-Norwegian Beamlines, ESRF for providing beamtime, and the staff; Wouter van Beek, Charles McMonagle, Dmitry Chernyshov and Vadim Dyadkin for their assistance during the beamtime.

Notes and references

1 M. Lilienblum, T. Lottermoser, S. Manz, S. M. Selbach, A. Cano and M. Fiebig, *Nat. Phys.*, 2015, **11**, 1070–1073.
2 S. H. Skjærvø, Q. N. Meier, M. Feygenson, N. A. Spaldin, S. J. L. Billinge, E. S. Bozin and S. M. Selbach, *Phys. Rev. X*, 2019, **9**, 031001.
3 A. Muñoz, J. A. Alonso, M. J. Martínez-Lope, M. T. Casáis, J. L. Martínez and M. T. Fernández-Díaz, *Phys. Rev. B*, 2000, **62**, 9498–9510.
4 S. C. Abrahams, *Acta Crystallogr. Sect. B Struct. Sci.*, 2001, **57**, 485–490.
5 A. S. Gibbs, K. S. Knight and P. Lightfoot, *Phys. Rev. B - Condens. Matter Mater. Phys.*, 2011, **83**, 094111.
6 S. Remsen and B. Dabrowski, *Chem. Mater.*, 2011, **23**, 3818–3827.
7 C. Abughayada, B. Dabrowski, M. Avdeev, S. Kolesnik, S. Remsen and O. Chmaissem, *J. Solid State Chem.*, 2014, **217**, 127–135.
8 S. H. Skjærvø, E. T. Wefring, S. K. Nesdal, N. H. Gaukås, G. H. Olsen, J. Glaum, T. Tybell and S. M. Selbach, *Nat. Commun.*, 2016, **7**, 13745.
9 Z. Liang, C. F. Yan, S. Rtimi and J. Bandara, *Appl. Catal. B Environ.*, 2019, **241**, 256–269.
10 S. F. Wang, H. Yang, T. Xian and X. Q. Liu, *Catal. Commun.*, 2011, **12**, 625–628.
11 M. Chen, B. Hallstedt and L. J. Gauckler, *J. Alloys Compd.*, 2005, **393**, 114–121.
12 N. Jiang, S. M. Woodley, C. R. A. Catlow and X. Zhang, *J. Mater. Chem. C*, 2015, **3**, 4787–4793.
13 J. S. Zhou, J. B. Goodenough, J. M. Gallardo-Amores, E. Morán, M. A. Alario-Franco and R. Caudillo, *Phys. Rev. B - Condens. Matter Mater. Phys.*, 2006, **74**, 1–7.
14 P. Gao, Z. Chen, T. A. Tyson, T. Wu, K. H. Ahn, Z. Liu, R. Tappero, S. B. Kim and S. W. Cheong, *Phys. Rev. B - Condens. Matter Mater. Phys.*, 2011, **83**, 1–9.
15 H. W. Brinks, H. Fjellvåg and A. Kjekshus, *J. Solid State Chem.*, 1997, **129**, 334–340.
16 K. Bergum, H. Okamoto, H. Fjellvåg, T. Grande, M.-A. Einarsrud and S. M. Selbach, *Dalt. Trans.*, 2011, **40**, 7583.
17 A. Muñoz, J. A. Alonso, M. T. Casais, M. J. Martínez-Lope, J. L. Martínez and M. T. Fernández-Díaz, *J. Phys. Condens.*

Please do not adjust margins

Please do not adjust margins

Matter, 2002, **14**, 3285–3294.
18 D. Okuyama, S. Ishiwata, Y. Takahashi, K. Yamauchi, S. Picozzi, K. Sugimoto, H. Sakai, M. Takata, R. Shimano, Y. Taguchi, T. Arima and Y. Tokura, *Phys. Rev. B - Condens. Matter Mater. Phys.*, 2011, **84**, 1–7.
19 B. L. Gersten, in *Crystal Growth Technology*, eds. K. Byrappa, W. Michaeli, E. Weber, T. Ohachi and H. Warlimont, William Andrew Inc., Norwich, NY, 2003, pp. 299–333.
20 E. D. Bøjesen and B. B. Iversen, *CrystEngComm*, 2016, **18**, 8332–8353.
21 O. G. Grendal, A. B. Blichfeld, T. D. Vu, W. van Beek, S. M. Selbach, T. Grande and M.-A. Einarsrud, *CrystEngComm*, 2019, **21**, 5922–5930.
22 B. L. Cushing, V. L. Kolesnichenko and C. J. O'Connor, *Chem. Rev.*, 2004, **104**, 3893–3946.
23 R. Dhinesh Kumar and R. Jayavel, *Mater. Lett.*, 2013, **113**, 210–213.
24 M. H. Harunsani, J. Li, Y. B. Qin, H. T. Tian, J. Q. Li, H. X. Yang and R. I. Walton, *Appl. Phys. Lett.*, 2015, **107**, 062905.
25 H. W. Zheng, Y. F. Liu, W. Y. Zhang, S. J. Liu, H. R. Zhang and K. F. Wang, *J. Appl. Phys.*, 2010, **107**, 053901.
26 E. S. Stampler, W. C. Sheets, W. Prellier, T. J. Marks and K. R. Poeppelmeier, *J. Mater. Chem.*, 2009, **19**, 4375–4381.
27 P. V Klevtsov and L. P. Sheina, *Izv. Akad. Nauk SSSR, Neorg. Mater.*, 1965, **1**, 912–917.
28 S. Mroczkowski, J. Eckert, H. Meissner, J. C. Doran and N. Haven, *J. Cryst. Growth*, 1970, **7**, 333–342.
29 K. P. Marshall, A. B. Blichfeld, S. L. Skjærvø, O. G. Grendal, W. van Beek, S. M. Selbach, T. Grande and M.-A. Einarsrud, *Chem. - A Eur. J.*, 2020, **26**, 9330–9337.
30 B. B. Van Aken, A. Meetsma and T. T. M. Palstra, *Acta Crystallogr. Sect. E Struct. Reports Online*, 2001, **57**, i87–i89.
31 O. M. Fedorova, V. F. Balakirev and Y. V. Golikov, *Inorg. Mater.*, 2011, **47**, 192–195.
32 V. F. Balakirev, O. M. Fedorova and Y. V. Golikov, *Dokl. Chem.*, 2009, **428**, 222–224.
33 J. D. Hancock and J. H. Sharp, *J. Am. Ceram. Soc.*, 1972, **55**, 74–77.
34 M. Avrami, *J. Chem. Phys.*, 1939, **7**, 1103–1112.
35 K. M. Ø. Jensen, C. Tyrsted, M. Bremholm and B. B. Iversen, *ChemSusChem*, 2014, **7**, 1594–1611.
36 X. W. Lou, Y. Wang, C. Yuan, J. Y. Lee and L. A. Archer, *Adv. Mater.*, 2006, **18**, 2325–2329.
37 B. Wang, H. Bin Wu, L. Zhang and X. W. Lou, *Angew. Chemie - Int. Ed.*, 2013, **52**, 4165–4168.
38 L. Cao, D. Chen and R. A. Caruso, *Angew. Chemie - Int. Ed.*, 2013, **52**, 10986–10991.
39 W. N. Budhysutanto, F. J. Van Den Bruele, B. D. Rossenaar, D. Van Agterveld, W. J. P. Van Enckevort and H. J. M. Kramer, *J. Cryst. Growth*, 2011, **318**, 110–116.
40 L. Jeuvrey, O. Peña, A. Moure and C. Moure, *J. Magn. Magn. Mater.*, 2012, **324**, 717–722.
41 S. L. Skjærvø, S. Sommer, P. Nørby, E. D. Bøjesen, T. Grande, B. B. Iversen and M.-A. Einarsrud, *J. Am. Ceram. Soc.*, 2017, **100**, 3835–3842.
42 A. A. Coelho, *J. Appl. Crystallogr.*, 2018, **51**, 210–218.
43 G. W. Beall, W. O. Milligan and H. A. Wolcott, *J. Inorg. Nucl. Chem.*, 1977, **39**, 65–70.
44 R. F. Klevtsova and P. V Klevtsov, *Zhurnal Strukt. Khimii*, 1964, **5**, 795–797.
45 G. Liu, W. Wong-Ng, J. A. Kaduk and L. P. Cook, *Phys. C Supercond. its Appl.*, 2010, **470**, 345–351.
46 A. C. Gaillot, V. A. Drits, A. Plançon and B. Lanson, *Chem. Mater.*, 2004, **16**, 1890–1905.
47 A. N. Christensen and B. Lebech, *Acta Crystallogr. Sect. B Struct. Crystallogr. Cryst. Chem.*, 1981, **37**, 425–427.
48 P. E. Blöchl, *Phys. Rev. B*, 1994, **50**, 17953–17979.
49 G. Kresse and J. Furthmüller, *Phys. Rev. B*, 1996, **54**, 11169–11186.
50 G. Kresse and D. Joubert, *Phys. Rev. B*, 1999, **59**, 1758–1775.
51 J. P. Perdew, A. Ruzsinszky, G. I. Csonka, O. A. Vydrov, G. E. Scuseria, L. A. Constantin, X. Zhou and K. Burke, *Phys. Rev. Lett.*, 2008, **100**, 1–4.
52 S. Dudarev and G. Botton, *Phys. Rev. B - Condens. Matter Mater. Phys.*, 1998, **57**, 1505–1509.
53 C. Degenhardt, M. Fiebig, D. Fröhlich, T. Lottermoser and R. V. Pisarev, *Appl. Phys. B Lasers Opt.*, 2001, **73**, 139–144.

 This journal is © The Royal Society of Chemistry 20xx

Please do not adjust margins